Journal of Computational Physics 231 (2012) 1533–1552

Contents lists available at SciVerse ScienceDirect

Journal of Computational Physics

journal homepage: www.elsevier.com/locate/jcp

A level set method for vapor bubble dynamics

Edip Can [a,1], Andrea Prosperetti [a,b,*]

[a] Faculty of Science and Technology and J.M. Burgers Centre for Fluid Dynamics, University of Twente, P.O. Box 217, 7500 AE Enschede, The Netherlands
[b] Department of Mechanical Engineering, Johns Hopkins University Baltimore, MD 21218, USA

ARTICLE INFO

Article history:
Received 26 May 2011
Received in revised form 13 October 2011
Accepted 18 October 2011
Available online 4 November 2011

Keywords:
Vapor bubble
Gas bubble
Explosive boiling
Free surface flow
Level set method

ABSTRACT

This paper describes a finite-difference computational method suitable for the simulation of vapor–liquid (or gas–liquid) flows in which the dynamical effects of the vapor can be approximated by a time-dependent, spatially uniform pressure acting on the interface. In such flows it is not necessary to calculate the velocity and temperature fields in the vapor (or gas). This feature simplifies the solution of the problem and permits the computational effort to be focussed on the temperature field, upon which the interfacial mass flux is critically dependent. The interface is described by a level set method modified with a high-order "subcell fix" with excellent mass conservation properties. The use of irregular stencils is avoided by suitably extrapolating the velocity and temperature fields in the vapor region. Since the accurate computation of momentum effects does not require the same grid refinement as that of the temperature field, the velocity field is interpolated on a finer grid used for the temperature calculation. Several validation and grid refinement axi-symmetric tests are described which demonstrate the intended first-order time, second-order space accuracy of the method. As an illustration of the capabilities of the computational procedure, the growth and subsequent collapse of a laser-generated vapor bubble in a microtube are described.

1. Introduction

Fixed grids are an attractive choice for the computation of free-surface flows due to their flexibility and efficiency, but they also give rise to very significant numerical problems which have generated a large literature.

In many of the proposed methods the interface is spread over a few computational cells (see e.g. [1,2]), or the density difference between the two fluids is artificially limited for numerical expediency [3]. Both features are undesirable in the case of flows in which vapor–liquid phase change processes are important as the accurate calculation of mass and heat fluxes at the interface is then of paramount importance. For this and other reasons several "sharp interface" methods have been devised such as the ghost-fluid method [4,5] and several variants of the volume of fluid (see e.g. [6–8]) and front tracking (see e.g. [9]) methods. In view of the connections with the present work, a particular mention is deserved by level-set methods implemented both with sharp (see e.g. [5,7,10]) and diffuse (see e.g. [2]) interfaces sometimes, as in the last paper cited, in combination with the volume-of-fluid method.

A central difficulty in the simulation of phase change processes stems from the small thermal diffusivity of liquids of common interest, in particular water, coupled with a large latent heat and a large difference between the liquid and vapor densities. Heat fluxes at the liquid–vapor interface are therefore large and capturing them correctly requires a very fine grid. For this reason, many of the available methods are illustrated with applications to fluids near the critical point, where the latent

* Corresponding author.
E-mail address: prosper@jhu.edu (A. Prosperetti).
[1] Present address: Saxion University of Applied Sciences, P.O. Box 70000, 7500 AE Enschede, The Netherlands.

0021-9991/$ - see front matter © 2011 Elsevier Inc. All rights reserved.
doi:10.1016/j.jcp.2011.10.021

heat is smaller and the phase densities closer, or to model problems. Exceptions are Refs. [7,10,11] in which the actual properties of water at normal pressure are used. In its most recent work this group has returned to a moving mesh [12].

A feature common to all these methods is their insistence on solving the Navier–Stokes equations in both the liquid and the vapor or gas phases. While this strategy endows them with a great generality and renders them able to deal with the density differences that one may encounter at very high pressures or close to the critical point, it fails to take advantage of the very significant simplification that is available in the much more common case in which the vapor density is several orders of magnitude smaller than the liquid one. In these situations, when the extent of the vapor space is limited, such as in the case of vapor bubbles, the most significant dynamical effect of the vapor is to provide a time-dependent, spatially uniform pressure on the liquid while its inertia and viscous stresses play a negligible role. Furthermore, the vapor temperature can also be assumed spatially uniform due to the very fast time scales for phase change and acoustic propagation.

This paper presents a numerical method suitable for these situations. Other problems to which it is equally applicable are encountered in the dynamics of gas bubbles and in other situations in which the pressure in the vapor or gas space can be assumed to be uniform. While we limit ourselves to axi-symmetric problems here, the method is readily extendable to three dimensions as well.

While abandoning the attempt to solve the vapor momentum equation limits the applicability of our method, the simplification to which it leads permits us to devise a more accurate solution procedure than possible with other methods, and in this aspect resides the usefulness of this work.

This study arose from an interest in the numerical solution of vapor–liquid flows encountered in microfluidic devices in some of which one takes advantage of the rapid and violent dynamics provided by vapor bubbles created by the intense local heating of small liquid masses in a confined environment. A well known example is the ink-jet printing process, in which the fast expansion of a vapor bubble in a narrow flow channel results in the ejection of a droplet of ink [13–16]. Other potential uses of vapor bubbles in small devices without mechanical moving parts include actuation [17,18], pumping [19,20], surface cleaning [21] and others. The performance of such devices is critically dependent on the bubble behavior which therefore needs to be understood from a fundamental viewpoint.

In the method described in this paper the liquid mass, momentum and energy equations are solved in cylindrical coordinates by means of a standard projection method on a uniform staggered grid. The vapor is modeled as a region of spatially uniform temperature, computed from an energy balance at the interface, and accompanying uniform saturation pressure which serves as a boundary condition for the liquid. The phase boundary is captured implicitly by means of the level set method. Discretization near the interface requires ghost values for the velocity in the vapor region. These values are generated by a procedure originally suggested in [22] modified according to the ideas of [23], which enforce the incompressibility constraint and properly account for viscous stresses at the interface.

Another feature of the method is that the energy equation is solved on a much finer grid than the momentum equation. This feature permits the accurate evaluation of temperature gradients at the interface, which are of paramount importance in establishing phase-change mass fluxes, while at the same time limiting the overall computational cost. A more detailed description of this and other features can be found in [24].

2. Mathematical formulation

We assume that velocities and temperature differences are sufficiently small that the liquid density and thermal properties can be treated as constants. The equations expressing the conservation of its mass, momentum and energy are therefore

$$\nabla \cdot \mathbf{u} = 0, \tag{1}$$

$$\frac{\partial \mathbf{u}}{\partial t} + \mathbf{u} \cdot \nabla \mathbf{u} = -\frac{1}{\rho}\nabla p + \frac{1}{\rho}\nabla \cdot \tau, \tag{2}$$

$$\frac{\partial T}{\partial t} + \mathbf{u} \cdot \nabla T = \alpha \nabla^2 T, \tag{3}$$

with $\mathbf{u}$, p, τ and T the liquid velocity, pressure, Newtonian viscous stress tensor and temperature fields, and ρ and α the liquid density and thermal diffusivity. Here and in the following liquid quantities are not subscripted; vapor quantities carry the subscript v, and quantities evaluated at the phase interface the subscript s.

Local temperature differences along the interface would give rise to evaporative or condensing mass fluxes able to equilibrate them on a smaller time scale than any other process under consideration. Furthermore, due to the very small vapor inertia, pressure gradients cannot persist beyond the acoustic time scale. The vapor phase is therefore modeled as a region with negligible inertia and spatially uniform pressure.

The balance of normal stresses at the interface is expressed by

$$p_v = p_s + \sigma\kappa - \mathbf{n} \cdot \tau_s \cdot \mathbf{n}, \tag{4}$$

where p_v is the vapor pressures, p_s the liquid pressure at the interface, σ the surface tension coefficient, κ the local curvature and $\mathbf{n}$ the unit normal directed into the liquid. Since the viscous stresses in the vapor are neglected, the liquid tangential stress at the interface must vanish:

$$\mathbf{t}\cdot\tau_s\cdot\mathbf{n}=0, \tag{5}$$

where $\mathbf{t}$ is the unit tangent vector to the interface.

We consider problems in which the rate of phase change is moderate and the vapor velocity is much smaller than the speed of sound so that we can assume thermodynamic equilibrium at the liquid–vapor interface. We therefore take p_v to be the saturation pressure at the interface temperature T_s. These two quantities are related by the Clausius–Clapeyron equation

$$\frac{dp_v}{dT_s}=\frac{L\rho_v}{T_s}, \tag{6}$$

with T_s is the interface temperature, L the latent heat of evaporation and condensation and ρ_v the vapor density. For simplicity, in this paper we use the perfect gas law for the vapor and assume L constant integrating this relation to find

$$p_v=p_{v,0}\exp\left[-\frac{L}{\mathcal{R}}\left(\frac{1}{T_0}-\frac{1}{T_s}\right)\right], \tag{7}$$

with $p_{v,0}$ and T_0 reference values for the vapor pressure and temperature and $\mathcal{R}$ the universal gas constant divided by the molecular mass of the vapor.

We show in the Appendix that, with the neglect of pressure gradients in the vapor, conservation of mass at the interface can be used to obtain the following relation for the surface temperature T_s:

$$\left(c_p+\frac{L^2}{\mathcal{R}T_s^2}-\frac{2L}{T_s}\right)\frac{dT_s}{dt}=\frac{1}{\rho_v V}\oint(k\nabla T\cdot\mathbf{n}-\rho_v L\mathbf{u}\cdot\mathbf{n})dS, \tag{8}$$

with c_p the liquid heat capacity at constant pressure. Due to the smallness of the vapor density, the term $\oint\mathbf{u}\cdot\mathbf{n}dS$ represents the rate of change of the vapor volume.

An even simpler situation to which the present method is applicable is that of liquid–gas problems with no phase change in conditions under which the gas pressure can be considered spatially uniform. An example is a gas bubble for which the gas pressure can often be adequately modelled by a polytropic pressure–volume relation (see Section 4).

3. Numerical method

The interface is described by a level set function ϕ. The numerical method makes use of a finite-difference discretization of the governing equations on a staggered MAC grid with equal spacings $\Delta r=\Delta z$ in the radial and axial directions; the scalar fields, namely pressure, temperature and level set function, are defined at cell centers, and the velocity components at the appropriate cell edges. As mentioned in the Introduction, the energy equation is solved on a grid finer than that used for the liquid velocity as described below.

The level set advection equation (see e.g. [25,26]) is updated in time by a second order Adams–Bashforth scheme

$$\frac{\phi^{n+1}-\phi^n}{\Delta t}=-\frac{3}{2}(\mathbf{u}\cdot\nabla\phi)^n+\frac{1}{2}(\mathbf{u}\cdot\nabla\phi)^{n-1}, \tag{9}$$

in which the superscripts denote time levels. The cell-center velocities are calculated by linear interpolation and the spatial derivatives of ϕ by a fifth-order WENO scheme [27–33]. The level set function is re-initialized at the end of the times step in order to preserve its signed distance nature by solving, in the artificial time τ [34],

$$\frac{\partial\phi}{\partial\tau}+S(\phi^0)(|\nabla\phi|-1)=0,\quad \phi(x,0)=\phi^0. \tag{10}$$

Here ϕ^0 is the level set function that results from the advection step (9) and $S(\phi^0)$ is a mollified sign function. This equation is integrated by the third order Runge–Kutta scheme of [30].

It is well known that use of the level set method can lead to a severe loss of mass. There have been several remedies proposed to ameliorate this problem (see e.g. [34–38]). We found the high-order version of [38] for the "subcell fix" proposed in [36] adequate for our purposes and, in particular, for the calculation of the curvature.

Because of the assumed symmetry of the problem, the liquid continuity and momentum equations are written in terms of ru_r in place of u_r (where r is the distance from the symmetry axis and u_r the radial velocity of the liquid) as suggested in [39]. The equations are integrated by a simple explicit first-order projection method (see e.g. [40–42]). The convection term is discretized by a second-order ENO method and the viscous terms are treated by central differencing. Although in an explicit scheme there would be no particular difficulty in accounting for the temperature dependence of the viscosity, for simplicity we do not include this effect in the representative results shown below.

Due to the explicit treatment of the convective and viscous terms the stability of the time integration requires a suitable limitation on the time step Δt. We set

$$\Delta t\left(\frac{1}{\tau_{conv}}+\frac{1}{\tau_{visc}}+\frac{1}{\tau_{surf}}\right)=\epsilon, \tag{11}$$

with $\epsilon = 0.25$, where τ_{conv}, τ_{visc}, τ_{surf} are the time scales for convection, diffusion and capillarity given by

$$\frac{1}{\tau_{conv}} = \frac{|u_r|_{\max}}{\Delta r} + \frac{|u_z|_{\max}}{\Delta z}, \quad \frac{1}{\tau_{visc}} = \frac{2\mu}{\rho}\left(\frac{1}{\Delta r^2} + \frac{1}{\Delta z^2}\right), \quad \frac{1}{\tau_{surf}} = \left(\frac{\sigma}{\rho \Delta r^3}\right)^{1/2}. \tag{12}$$

3.1. Pressure Poisson equation with Dirichlet condition

One difference between the present problem and other implementations of the projection method is that the pressure Poisson equation needs to be solved subject to a specified pressure at the interface. The method developed in [43] is used to avoid the need for irregular stencils near the interface.

Consider for example the situation depicted in Fig. 1 where the interface cuts between the node $(i-1,j)$ in the vapor and (i,j) in the liquid. In order to impose the pressure condition $p = p_s$ at the interface, with p_s given by (4), we introduce a ghost pressure p^{ghost} at $(i-1,j)$ using linear extrapolation:

$$p^{\text{ghost}}_{i-1,j} = p_{i,j} - \frac{p_{i,j} - p_s}{\theta \Delta r}\Delta r = \frac{p_{i,j}(\theta - 1) + p_s}{\theta}, \tag{13}$$

where θ is the fraction of grid spacing between the node (i,j) and the interface. Inserting this expression into the standard discretization of the Poisson equation results in

$$(\nabla^2 p)_{i,j} = \frac{1}{r_{i,j}\Delta r^2}\left[r_{i+1/2,j}(p_{i+1,j} - p_{i,j}) - r_{i-1/2,j}\frac{p_{i,j} - p_s}{\theta}\right] + \frac{1}{\Delta z^2}\left[(p_{i,j+1} - p_{i,j}) - (p_{i,j} - p_{i,j-1})\right]. \tag{14}$$

The term containing the interface pressure, p_s, is known and can therefore be taken to the right-hand side of the Poisson equation. This procedure permits us to construct the system matrix by applying the standard discretization to all grid cells irrespective of whether they are cut by the interface or not. The resulting matrix is symmetric and the linear system is solved by the conjugate gradient method. When θ is close to zero, the interface is very near a grid point. In this case the pressure at that grid point can be considered known and taken equal to that at the interface with negligible error. After several numerical tests we have found that taking this step when $\theta \leqslant 0.01$ is satisfactory.

After solving for the pressure field, the pressure gradient is needed for the velocity correction step. Consider the left panel of Fig. 1. To calculate the pressure gradient at the node $Q = (i-1/2,j)$ we use the one-sided formula

$$\left(\frac{\partial p}{\partial r}\right)_{i-1/2,j} \simeq \frac{p_{i,j} - p_s}{\theta \Delta r}. \tag{15}$$

The same formula can be used to calculate the pressure gradient at the node Q in the right panel which lies in the vapor. In this way we can consistently apply the standard liquid velocity correction of the projection method at such nodes where the intermediate velocity u_r^* is calculated from the extrapolated velocity field at the previous time step.

3.2. Velocity extrapolation

To avoid the use of irregular stencils for the velocity discretization in the neighborhood of the interface we extrapolate the liquid velocity field into the vapor region. This extrapolation procedure is one of the significant features of our method.

There are several ways in which the velocity can be extrapolated on the other side of the interface (see e.g. [4]). As noted by [44,23], however, a shortcoming of many methods is that they violate the incompressibility constraint, with a consequent degradation of the reconstruction of the interface. Here we extend the method proposed for inviscid flows in [23] to the viscous case and account for the zero-tangential-stress condition (5) by means of a Lagrange multiplier in the manner developed in [22].

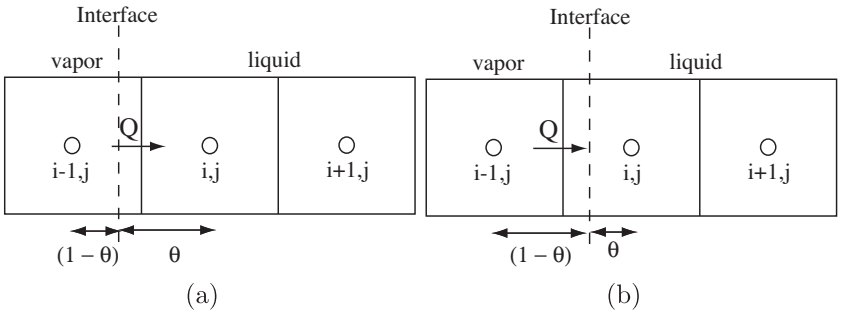

Fig. 1. Interface between nodes $(i-1,j)$ and (i,j); θ denotes the distance from the liquid node (i,j) to the interface in terms of the grid spacing and ranges from 0 to 1.

The key idea put forward in [23] is to enforce the incompressibility of the extrapolated velocity in the same way in which the provisional velocity $\mathbf{u}^\star$ of the projection method is rendered divergenceless. Thus, the extrapolation procedure consists of three steps. First, the liquid velocity field is extrapolated linearly into the vapor by means of the least squares method. Then, an auxiliary pressure in the extrapolated region is found by solving a Poisson equation with the divergence of the linearly extrapolated velocity as the source term. Finally, the gradient of this auxiliary pressure is used to correct the extrapolated velocity so that it is rendered divergenceless.

We explain these steps in succession with reference to Fig. 2. Suppose it is desired to extrapolate a velocity component to the point marked by X. For this purpose we use valid velocities at neighboring liquid nodes, i.e. velocities at nodes where the momentum equation was solved (including nodes such as Q in Fig. 1 right or Z in Fig. 2). To identify these nodes we first estimate the coordinates of the interface point P closest to X from

$$r_P = r_X + |\phi_X| \cos\beta \quad z_P = z_X + |\phi_X| \sin\beta, \tag{16}$$

where the subscripts X and P identify the points in question and $|\phi_X|$ is the distance between them in view of the signed distance property of the level set function and the fact that $\phi_P = 0$ as it lies on the interface. The angle β is the angle between the normal vector through X, estimated from $\nabla\phi_X$, and the radial direction. The radial liquid velocity component closest to P, labeled by Y in the figure, is then found by searching in a small neighborhood around P. After this step, a search is performed in a square region of size 5×5 cells centered at Y (dashed square in the figure). All the valid radial and axial velocity components within this square are selected for the velocity extrapolation. We approximate the velocity field in this region as

$$\mathbf{u}^{\text{ext}} = \mathbf{A} \cdot \mathbf{x} + \mathbf{u}_P, \tag{17}$$

where

$$\mathbf{x} = (r - r_P, z - z_P), \quad \mathbf{u}_P = (u_{r,P}, u_{z,P}) \tag{18}$$

and

$$\mathbf{A} = \begin{pmatrix} a_{rr} & a_{rz} \\ a_{zr} & a_{zz} \end{pmatrix}. \tag{19}$$

The quantities a_{ij} would be the velocity derivatives at P if the linear approximation (17) were exact.

The problem therefore is to find the matrix $\mathbf{A}$ and vector $\mathbf{u}_P$ that give the best approximation to the liquid velocity components within the dashed region, after which (17) can be used to assign a (provisional) value to the velocity at X. This amounts to minimizing

$$\mathcal{L}_0 = \sum_{K=1}^{N} [a_{rr}(r_K - r_P) + a_{rz}(z_K - z_P) + u_{r,P} - u_{r,K}]^2 + \sum_{K=1}^{M} [a_{zr}(r_K - r_P) + a_{zz}(z_K - z_P) + u_{z,P} - u_{z,K}]^2, \tag{20}$$

where N and M are the number of valid radial and axial velocity components within the 5×5 region and $u_{r,K}$ and $u_{z,K}$ are the valid radial and axial velocity components. The extrapolated velocity field should satisfy the zero tangential stress condition (5) on the interface. This constraint can be written in terms of the approximate spatial derivatives of the velocity components as

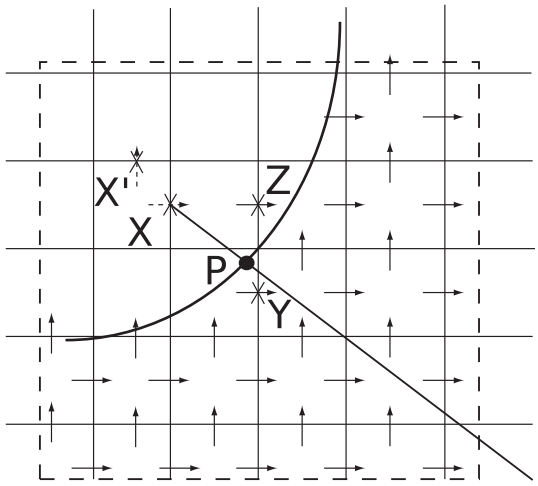

Fig. 2. Selection of nodes for the extrapolation of the liquid velocity into the vapor region. The points marked X and X' are those where an extrapolated radial velocity is desired. The point P is found by drawing the normal to the interface from X. An area of 5×5 cells centered at P is searched for nodes with a liquid velocity obtained from the momentum equation. All these nodes are used in the least squares fit.

$$Q = 2n_r t_r a_{rr} + (n_r t_z + n_z t_r)(a_{rz} + a_{zr}) + 2n_z t_z a_{zz} = 0, \tag{21}$$

where n_r, t_r and n_z, t_z are the radial and axial components of the normal and tangent unit vectors, respectively. Since the normal at P has the same direction as at X, the tangent at P can be equally well calculated as the direction perpendicular to the line XP at X. Furthermore, the velocity gradients a_{ij} are locally constant and therefore have the same value at P as at X. Thus, while in principle (21) should be evaluated at P, its value at X is exactly the same. The constraint (21) can be added to (20) to find

$$\mathcal{L} = \mathcal{L}_0 + \lambda Q, \tag{22}$$

where λ is a Lagrange multiplier. Minimizing $\mathcal{L}$ gives 7 equations for the seven unknowns a_{ij}, $u_{r,P}$, $u_{z,P}$ and λ after which the radial velocity at X is evaluated from (17). We use the same equation to calculate the axial velocity component carrying the same indices, i.e., the velocity u_z at the node marked X' in Fig. 2. This procedure arbitrarily privileges the radial velocity components, but we have found essentially the same results by centering the extrapolation at the axial velocity points such X' in Fig. 2. This extrapolation is carried out in vapor region satisfying $-J\Delta r < \phi < 0$ with J typically taken equal to 5.

To make the extrapolated velocity field divergence-free we use a projection step based on an auxiliary pressure field p^{aux} in the extrapolated vapor region obtained by solving

$$\nabla^2 p^{\mathrm{aux}} = \nabla \cdot \mathbf{u}^{\mathrm{ext}}, \tag{23}$$

where $\mathbf{u}^{\mathrm{ext}}$ denotes the extrapolated velocity as determined by the previous procedure. The equation is solved only for the nodes at which the velocity was extrapolated. The boundary of this region on the liquid side is constituted by cell edges with velocity components determined from the momentum equation. These velocity components do not need to be corrected and therefore homogeneous Neumann conditions on p^{aux} are imposed there. Following [23], homogeneous Dirichlet conditions are imposed on p^{aux} at the boundary of the velocity extrapolation region on the vapor side.

3.3. Energy equation

In the situations of our primary concern the entire flow is critically dependent on the phase change taking place at the vapor–liquid interface which, in turn, hinges on an accurate evaluation of the temperature gradient. With the rapid transients characteristic of many vapor bubble problems, thin thermal boundary layers develop the resolution of which requires a very fine discretization. Viscous boundary layers, on the other hand, tend to be thicker as inertia limits the time scale for liquid motion and, furthermore, viscous effects are less critical to the system's dynamics. Additionally, phase change often leads to large thermal gradients which, therefore, are mostly localized near the interface. These considerations suggest that, while a relatively coarse grid is sufficient for the momentum equation, a fine grid is necessary for the energy equation near the interface. Furthermore, since this fine grid need not extend over the entire domain, one can make an efficient use of computational resources determining the temperature field and its gradients with great accuracy while enjoying, at the same time, the simplifications stemming from the use of a uniform non-adaptive grid.

Thus, we use two computational domains, a larger one, the momentum domain, on which the mass and momentum equations are solved, and a smaller energy domain, localized near the interface, on which the energy equation is solved. The size of the thermal domain depends on the type of problem, the only requirement being that its outer boundary remain in a liquid region where the temperature is substantially unaffected by the interfacial processes. A suitable position for this outer boundary may be established a priori by physical arguments, or determined by running coarsely resolved exploratory calculations. Since velocity gradients are much smaller than temperature gradients, and incompressibility is not a critical issue for the solution of the energy equation, the velocity field available on the momentum grid can be simply interpolated to the thermal grid. We use linear interpolation for both the velocity field and the level set function.

An illustration is given in Fig. 3 which shows the grids used in the spherical vapor bubble collapse described later in Section 4. The momentum domain extends to 5 times the initial bubble radius. A thermal domain extending to only 1.5 times the bubble radius however proves sufficient. The resolution of the thermal domain shown here is 4 times higher than that used for the momentum domain. We have tested refinements of 2, 4, 8 and 16 times with respect to the momentum grid and the results of these tests are described later.

For the sake of stability, and in order to avoid the need for excessively short time steps, it is desirable to use an implicit discretization of the energy equation. In place of the usual Crank–Nicholson scheme, for reasons explained below, we use a fully implicit discretization of the diffusion term:

$$\frac{T^{n+1} - T^n}{\Delta t} + (\mathbf{u} \cdot \nabla T)^n = \alpha\left(\nabla^2 T^{n+1}\right). \tag{24}$$

This equation is solved by the conjugate gradient method. We use the Dirichlet condition to assign ghost values to the vapor nodes adjacent to the interface in the same way described before for the pressure. With these ghost values, a standard finite-difference discretization of the diffusion term of (24) is possible. For the convective term a second order ENO scheme is used, which requires fictitious temperatures in the vapor region at distances of up to two cells from the interface. To generate these values, the temperature field at time level t^n is extrapolated linearly in the normal direction. For this purpose, first the liquid-side temperature gradient normal to the interface, $\mathbf{n} \cdot \nabla T^n$, is propagated as a constant using the method based on a first-order PDE developed in [45]. The interfacial values are found from ∇T^n in a dimension-by-dimension manner as

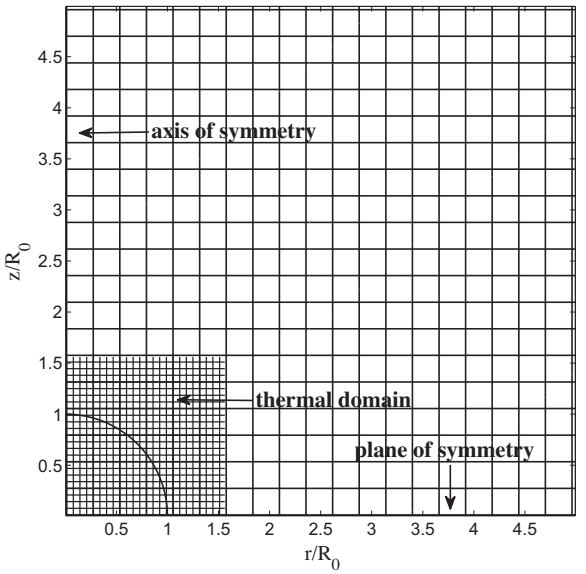

Fig. 3. The momentum and thermal grids used for the simulation of a condensing vapor bubble. Only 1 in 20 grid lines are shown for clarity. The thermal domain can be taken relatively small due to the presence of a thin thermal boundary layer. Hence the thermal resolution can be high without a significant increase in computational effort.

illustrated in Fig. 4. Here the radial derivative is calculated by using nodes A and B and the axial derivative by using nodes A and C, rather than D, as C is closer to the interface. Temperature values for grid points in the vapor phase close to the interface may then be defined using the interface temperature, T_s, and the extrapolated normal gradients as $T^n_{i,j} = T^n_s + \phi^n_{i,j}(\mathbf{n}\cdot\nabla T)^n_{i,j}$ in view of the signed distance nature of the level set function ϕ. This extrapolation step is also useful when a node transitions from the vapor to the liquid between t^n and t^{n+1} and a liquid value for T^n is needed for the discretization of the time derivative. We have not used the Crank–Nicholson temporal discretization of the diffusion term to avoid the need for temperature information from one node layer farther into the vapor, which would be necessary when the interface traverses a grid line between t^n and t^{n+1}.

As the thermal grid spacing is smaller than the momentum grid spacing, the convective time scale in (12) is computed using the thermal grid size Δr_{therm}.

In summary, the computational sequence proceeds along the following steps:

1. advance the liquid–vapor interface by integrating the level set equation;
2. re-initialize the level set function by driving the solution to (10) to steady state in the pseudo-time τ;
3. compute the thermal gradient normal to the interface and extrapolate the liquid temperature into the vapor region;
4. compute the new surface temperature from (8) by a first-order explicit stepping and, from it, the new vapor pressure from (7). The temperature so computed serves as boundary condition for the interface;
5. solve the energy Eq. (3);

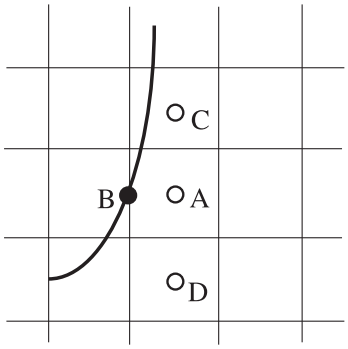

Fig. 4. Illustration of the procedure for the calculation of the normal temperature gradient at the interface. The radial component is calculated from the temperatures at A and B, the axial component from the temperatures at A and C.

6. solve the momentum equation by means of the projection method;
7. extrapolate the new velocity field into the vapor region enforcing the interface stress condition and incompressibility;
8. go back to step 1.

4. Verification

For the verification of the numerical method described in Section 3 we performed simulations of the damped volume oscillations of a gas bubble, of the growth of a vapor bubble in a superheated liquid and of the collapse of a vapor bubble in a subcooled liquid.

4.1. Volume oscillations of a gas bubble

The radial dynamics of a bubble in an unbounded liquid are governed by the well-known Rayleigh–Plesset equation [46] which is suitable for a spherical bubble surrounded by an infinite liquid expanse. A fair comparison of our numerical method with the results of this equation would require the use of a very large computational domain. For this reason, we use a form of the Rayleigh–Plesset equation modified so as to account for a finite amount of liquid surrounding the bubble; this equation is [47,48]

$$\frac{S-R}{S}\left\{R\frac{\mathrm{d}^2R}{\mathrm{d}t^2}+\left[2-\frac{(S^2+R^2)(S+R)}{2S^3}\right]\left(\frac{\mathrm{d}R}{\mathrm{d}t}\right)^2\right\}=\frac{1}{\rho}\left[p_g-p_\infty-\frac{2\sigma}{R}-\frac{4\mu}{R}\frac{\mathrm{d}R}{\mathrm{d}t}\right], \tag{25}$$

in which R is the instantaneous bubble radius, p_g the bubble internal pressure and S the radius of a concentric spherical surface on which the ambient pressure p_∞ is imposed. For the present purposes it suffices to compute the gas pressure from a simple model; we use the relation for an adiabatic perfect gas

$$p_g=p_{eq}\left(\frac{R_{eq}}{R}\right)^{3\gamma}, \tag{26}$$

in which the subscripted quantities are the values at equilibrium and $\gamma=1.4$ is the gas adiabatic index. In our calculation we take $R_{eq}=23.75$ μm and $S/R_{eq}\simeq 11.45$, which gives a total liquid volume close to that of our computational domain which, because of symmetry, is one quarter of a meridian plane extending 10 bubble radii in the r- and z-directions (see Fig. 3). On the outer boundary of the computational domain we prescribe $p=p_\infty$ and zero normal gradients of the velocity. The bubble is initialized with a radius $R_0=25$ μm so that it is slightly over-expanded with respect to its equilibrium radius causing it to execute volume oscillations damped by the liquid viscosity μ. The liquid properties are those of water at 101 kPa pressure and 20 °C: $\rho=10^3$ kg/m^3, $\mu=10^{-3}$ kg/m s and $\sigma=0.073$ N/m. In the presentation of results we use a dimensionless time defined by $t^\star=\sqrt{p_\infty/\rho}\,t/R_{eq}$.

In order to determine the temporal accuracy of the method we perform four simulations with varying constant time steps. The computational grid for these computations comprised of 256×256 cells so that the grid spacing is $\Delta r/R_{eq}=0.039$. Fig. 5 shows the result of the direct integration of Eq. (25) together with the results of the simulations carried out with the smallest and largest time steps, $\Delta t^*=10^{-3}$ and $\Delta t^*=2\times10^{-2}$. We define error norms by

$$L_1=\frac{\sum|f^r-f|}{\sum|f^r|},\quad L_2=\frac{(\sum|f^r-f|^2)^{1/2}}{(\sum|f^r|^2)^{1/2}}, \tag{27}$$

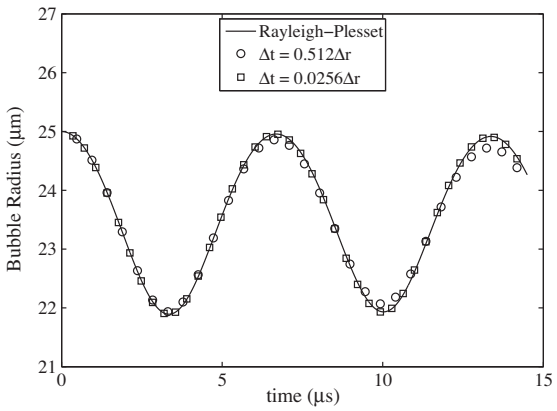

Fig. 5. Comparison of the radius of a gas bubble executing damped radial oscillations as calculated from the modified Rayleigh–Plesset Eq. (25) (solid line) and by the present method with a fine (squares) and coarse (circles) time resolution.

in which f is either the pressure or one of the velocity components and the superscript r denotes the reference value, for which we take the results obtained with the smallest time step. The summation is carried out over all grid points that lie in the liquid region, i.e. all points that satisfy $\phi > 0$. Table 1 shows the L_1 and L_2 norms for the pressure and both velocity components as well as the rate of convergence. These values were calculated at a non-dimensional time $t^* = 6$. The temporal convergence rate is slightly greater than 1.

The spatial convergence rate is determined by performing simulations with varying grid resolutions, keeping the time step fixed at $0.0512\Delta r^{min}/R_{eq} = 10^{-3}$, in which Δr^{min} is the mesh length of the finest grid used. The norms are calculated by means of bilinear interpolation between grids. Fig. 6 shows the error norm as a function of grid size on a bi-logarithmic scale for the radial velocity component. As expected, the spatial accuracy is very close to second order.

In the present algorithm the interface velocity can be calculated in two ways, either by following the zero-level-set points or by interpolating the liquid velocity between the value at the node closest to the interface and the extrapolated value in the bubble. We have found that the two results agree very closely, which proves the accuracy of the velocity extrapolation procedure. Fig. 7 compares the two components of the numerical velocity at the bubble surface with the analytic values given by $u_r = \dot{R}\cos\theta$ and $u_z = \dot{R}\sin\theta$ at the non-dimensional time $t^* = 2.25$, at which the radius and velocity are $R/R_{eq} = 1.012$ and $\sqrt{\rho/p_\infty}\dot{R} = 0.127$. The comparison is excellent.

4.2. Vapor bubble growth

The previous example illustrates the accuracy of the coupling between the level-set formulation and the momentum equation. We now describe an example to demonstrate the performance of the energy–momentum coupling. For this purpose we consider a spherical bubble at rest in a liquid at temperature $T_\infty = 105$ °C, initially at the saturation pressure, which becomes superheated by a gradual decrease of the ambient pressure according to

$$p_\infty(t) = p_{sat}(T_\infty) - (1 - e^{-t/\tau})\Delta p. \tag{28}$$

As a consequence, the bubble starts to grow in a gradually developing temperature distribution. We take $\Delta p = 19.5$ kPa, corresponding to a superheat of 5 °C, and $\tau = 5t_c$, with t_c a characteristic time given by (see e.g. [49,51])

$$t_c = \frac{\pi R_0^2}{4Ja^2\alpha}, \tag{29}$$

in which $Ja = \rho c_p \Delta T/L\rho_v$ is the Jakob number; for this case $t_c = 51.19$ μs so that $\tau = 0.256$ ms. The initial radius is $R_0 = 50$ μm. We compare the results of the present method with those obtained from the method described and extensively validated in [50], whose original code was adapted for the present purposes.

The computational domain is a cylinder with radius and height equal to 16 times the initial bubble radius R_0 discretized with a mesh $\Delta r = \Delta z = R_0/32$. The domain for the energy equation can be taken much smaller as the temperature varies only in the close neighborhood of the bubble. We take it to extend to only twice the initial radius with cells 16 times smaller than the momentum cells so that each momentum cell contains 256 thermal cells. The outer boundary of the computational domain is treated as in the previous example except that the pressure is given by (28) rather than being constant. The physical properties of the liquid are those of water at 101 kPa and 373.15 K: $\rho = 955.1$ kg/m^3, $\mu = 2.67 \times 10^{-4}$ kg/ms, $k = 0.68$ W/m, $\alpha = 1.69 \times 10^{-7}$ m^2/s, $L = 2257 \times 10^3$ J/kg and $\sigma = 0.059$ N/m. The simulation is stopped when R becomes close to $2R_0$ as the thermal grid does not extend farther.

Because of the surface tension over-pressure, the initial vapor pressure is insufficient for equilibrium and the bubble initially shrinks slightly, causing a temporary condensation and attendant pressure increase. This process causes it to rebound, after which growth starts in response to the falling ambient pressure.

Fig. 8(a) and (b) compare the bubble radius and radial velocity given by the present method (solid lines) with those of the method of Ref. [50]. The results for the radius are essentially superposed within the thickness of the lines. A close inspection of the figure for the velocity shows a slight difference near the initial minimum, and a more noticeable difference toward the

Table 1
L_1 and L_2 norms for the pressure, radial and axial velocity components.

	Δt_1	Δt_2	Δt_3	Δt_4	Order
Pressure					
L_1	1.402e−4	3.847e−4	8.648e−4	1.794e−3	1.23
L_2	2.523e−4	6.919e−4	1.555e−3	3.224e−3	1.23
Radial velocity component					
L_1	9.566e−3	2.644e−2	5.937e−2	1.206e−1	1.22
L_2	1.147e−3	3.162e−3	7.092e−3	1.441e−2	1.21
Axial velocity component					
L_1	9.629e−3	2.653e−2	5.947e−2	1.208e−1	1.21
L_2	1.151e−3	3.166e−3	7.103e−3	1.443e−2	1.21

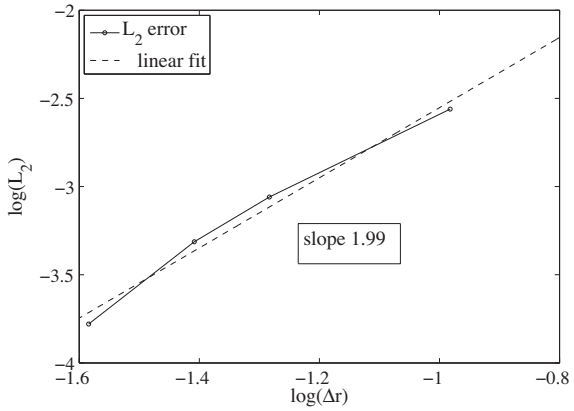

Fig. 6. L_2 error norm for the radial velocity of a gas bubble executing damped radial oscillations as a function of the grid size. The dashed line, with a slope very close to 2, is a linear fit.

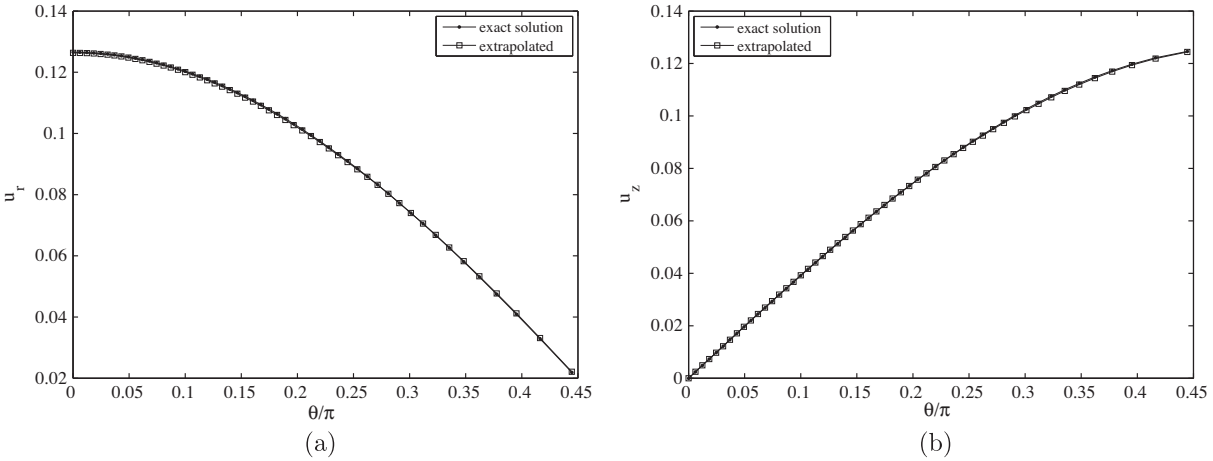

Fig. 7. Comparison between the analytic (solid lines) and numerical velocity components along the interface of a gas bubble executing damped radial oscillations; (a) radial component, (b) axial component.

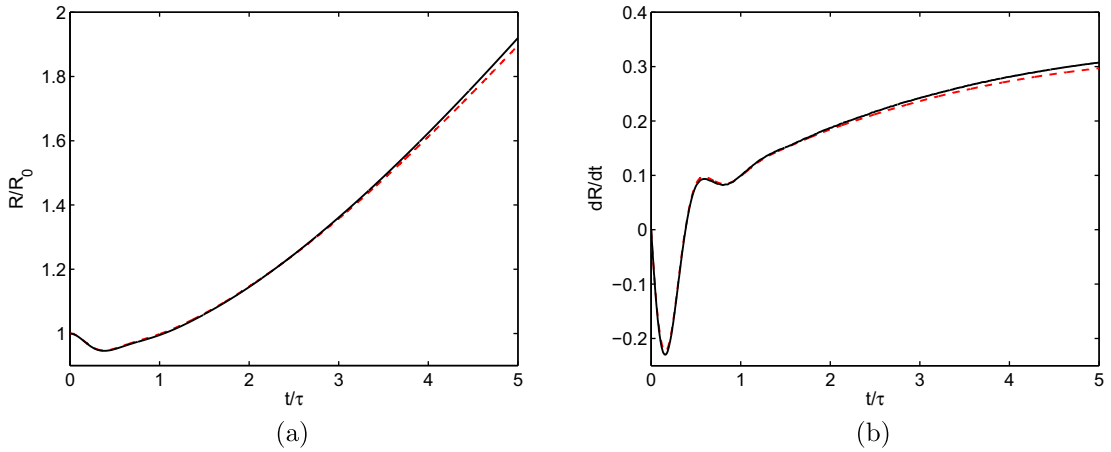

Fig. 8. Normalized radius (left) and velocity of a growing vapor bubble in a superheated liquid as given by the present method (solid lines) compared with the benchmark solution of [50]. As the bubble grows the effect of the finite domain size becomes more noticeable.

end of the simulation. The former is due to the smaller liquid inertia caused by the finite size of the computational domain, as opposed to the infinite one implied by the use of the Rayleigh–Plesset equation. To prove this statement we have carried out the same simulation on a computational domain only 8 times larger than the initial radius. On this latter domain the minimum dimensionless velocity was -0.2380, while it was -0.2300 on the larger domain. Linear extrapolation to an infinite domain size predicts a minimum velocity of -0.2220, to be compared with the value -0.2234 given by the Rayleigh–Plesset simulation. At later times, this inertial effect compounds with the gradual approach of the bubble surface to the edge of the energy domain (equal to twice the initial radius R_0), which decreases the accuracy of the temperature calculation. These effects cause the more noticeable differences appearing for $t/\tau > 3$.

Fig. 9 compares the vapor pressure as given by the two models. We do not show a comparison of the temperatures as the two lines are indistinguishable. As a consequence of the initial shrinkage of the bubble and consequent vapor condensation, the surface temperatures rises slightly and, with it, the internal pressure. Both quantities start to decline as the ambient pressure decreases and the growth proceeds.

4.3. Collapsing vapor bubble in a subcooled liquid

We now consider the converse process of the collapse of a spherical vapor bubble in an unbounded subcooled liquid. Far away from the bubble the pressure is 101 kPa. If the bubble is to collapse, the liquid should be subcooled. This requirement poses a delicate numerical challenge as vapor starts to condense as soon as the bubble wall begins its inward motion causing the immediate formation of an unresolvably thin thermal boundary layer. In this situation it is impossible to produce grid-independent results. This difficulty can be circumvented by using a gradually increasing ambient pressure, similarly to the procedure used in the previous example, or by starting with an initial, non-uniform liquid temperature distribution. Here we follow the latter route and take

$$T(r,z,0) = T_\infty + \Delta T \exp\left(-\frac{\sqrt{r^2+z^2}-R_0}{\delta}\right), \tag{30}$$

with $\Delta T = 3.35$ K the initial subcooling, $R_0 = 1$ mm and $\delta = 0.001R_0$ the thickness of the initial boundary layer. The physical properties of the liquid are those of water at 101 kPa and 373.15 K. The computational domain on which the momentum equation is solved extends to 5 times the initial bubble radius, with a grid spacing $\Delta r/R_0 = 0.013$. Since the bubble radius decreases in this process, the domain for the energy equation is taken to extend to only 1.5 times the initial bubble radius. The grid spacing for the energy equation is varied by taking 1/2, 1/4, 1/8 and 1/16 of $\Delta r/R_0$.

The bubble volume and vapor temperature during the early stages of collapse are shown in Fig. 10(a) and (b). This volume is normalized by the initial volume $V_0 = \frac{4}{3}\pi R_0^3$ and the time by t_c defined in (29), which is the estimate of the collapse time of a stationary spherical vapor bubble given by Florschuetz and Chao [49]; in the present case $t_c \simeq 46.46$ ms. Both the volume and the surface temperature exhibit some oscillations in the early stages of the collapse, due to the competing effects of phase change and inertia, as already found in [50,51].

For the coarsest grid there is only one node in the initial boundary layer. As the grid is refined this number increases until, as can be seen from Fig. 10, the results for thermal grid spacings of $\Delta r/8$ and $\Delta r/16$ become nearly coincident, which proves convergence with grid refinement. This convergence is seen more clearly in panel (c) where the bubble volume data from the

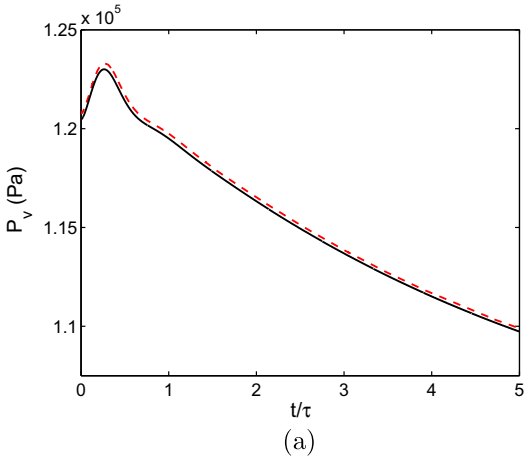

Fig. 9. Vapor pressure inside the growing bubble of the previous figure. The solid line is the result of the present method and the dashed line the benchmark solution of [50].

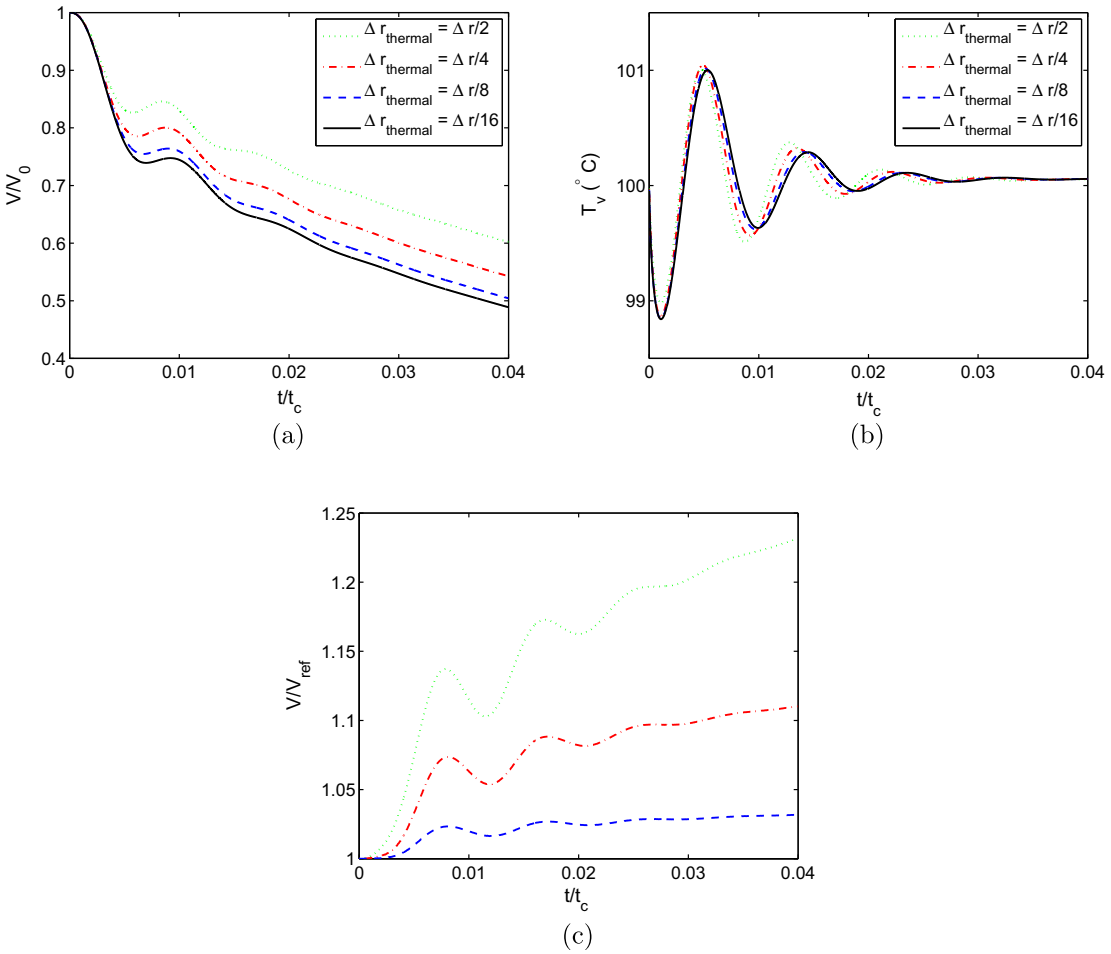

Fig. 10. (a) Normalized volume of a collapsing vapor bubble in a subcooled liquid; (b) bubble surface temperature; (c) ratio of the instantaneous bubble volume for the three coarser thermal grid resolutions to the value found with the finest resolution. In all these figures the small oscillations are a physical effect due to the competition between inertial and thermal processes as explained in the text.

three coarser thermal grid resolutions are normalized with the results of the finest resolution. The difference between the two finest resolutions is less than 3%.

During the collapse the bubble remains substantially spherical as shown by the thick black lines in Fig. 11. The other lines in these panels show isotherms at four instants during the collapse, $t/t_c = 0.06, 0.13, 0.20$ and 0.27. These lines are very close to concentric circles as they should.

5. Application: laser-generated vapor bubble in a tube

We now briefly describe the application of the previous method to the vapor bubble generated by a laser pulse focused on the mid-plane of a liquid-filled microtube. After the laser flash, the bubble undergoes a period of fast growth followed by a relatively slow collapse. The results of experiments and a simple model for this problem were described in [52] and a more detailed numerical investigation can be found in [24].

5.1. Simulation setup

We consider a cylindrical tube of diameter D, open at the two ends, containing a liquid column with length $2H$. We take advantage of symmetry to consider only one half of the physical problem; a schematic of the computational domain is shown in Fig. 12, which also shows the velocity boundary conditions. Since we need a few nodes to remain in the liquid for the purpose of velocity extrapolation, as already done in [53], we set to zero the radial velocity of the bubble interface when it gets very close to the tube wall. As the radial velocity field in this region is already extremely small, this procedure has a

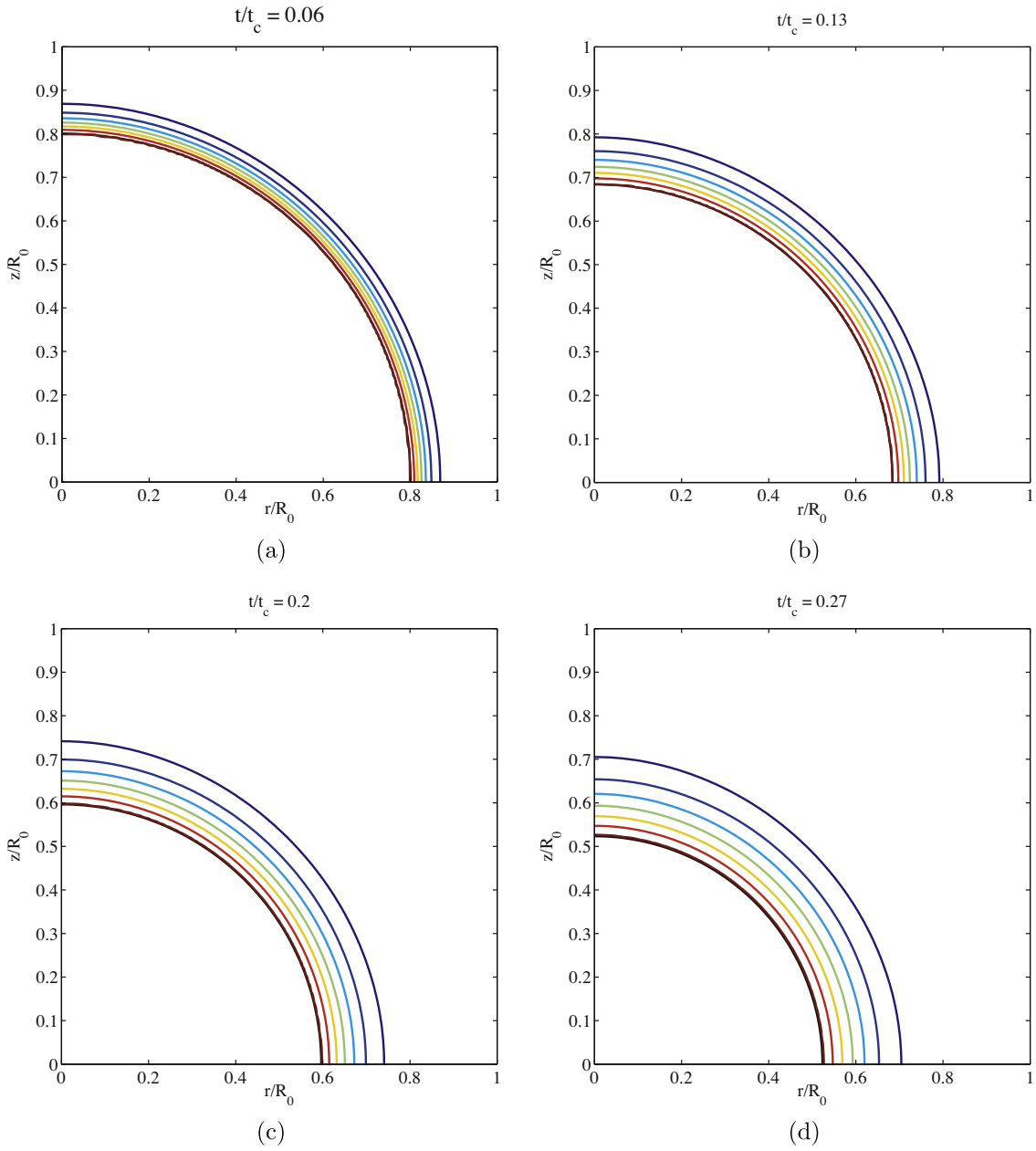

Fig. 11. Bubble interface (solid black line) and liquid isotherms at four instants during the collapse of a vapor bubble in a subcooled liquid. The temperature isotherms vary from T_∞ = 96.65 °C to 100 °C.

negligible influence on the results. On the computational boundary corresponding to the end of the liquid column the pressure is kept at the reference value and the velocity gradients normal to the computational boundary are set to zero.

During the whole growth and collapse process, the temperature only varies in the close neighborhood of the bubble. The size of the energy domain needed was estimated by a preliminary low-resolution simulation as mentioned before. The temperature at the top boundary of the energy domain is kept at the reference value T_∞. The tube wall is assumed to be adiabatic.

The tube diameter D is taken as the characteristic length scale of the problem. The liquid column has length $2H$ and $\mathcal{A} = H/D$ is the aspect ratio of the liquid mass. Following [53], a scale for the velocity is defined by means of a simple consideration in which the bubble pushes a liquid column of length H. Taking the initial vapor pressure above p_∞, Δp, as the force per unit area that pushes the liquid, an acceleration can be defined as $\Delta p/\rho H$, on the basis of which we define a velocity scale by multiplying by the length scale, D, and taking the square root:

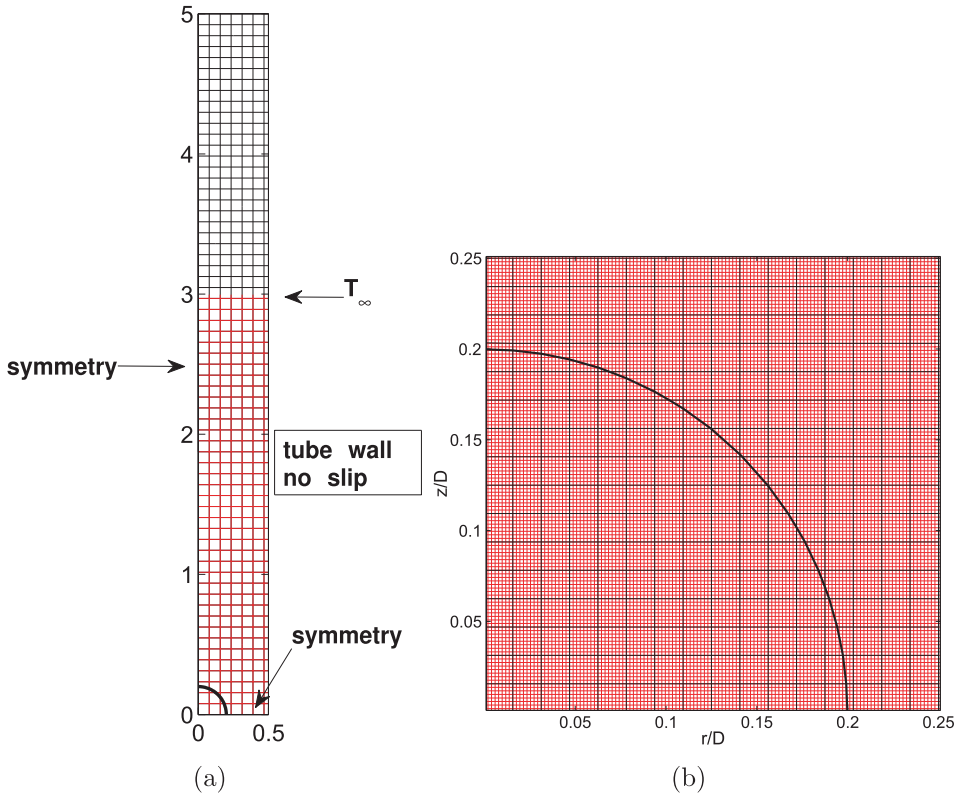

Fig. 12. (a) Schematic of the computational domain used in the simulation of the growth and collapse of a laser-generated vapor bubble. A few lines of the momentum (black) and thermal (red) grids are shown. The initial bubble is also indicated by the black curve. (b) The actual momentum and thermal grid lines near the bubble. The thermal grid has a resolution 8 times higher than the momentum grid. (For interpretation of the references to colour in this figure legend, the reader is referred to the web version of this article.)

$$V = \sqrt{\frac{\Delta p D}{\rho H}} = \sqrt{\frac{\Delta p}{\rho \mathcal{A}}}. \tag{31}$$

A time scale t_s is defined from the length and velocity scales:

$$t_s = \frac{D}{V} = D\sqrt{\frac{\rho \mathcal{A}}{\Delta p}}. \tag{32}$$

Using these scales Reynolds, Weber and Péclet numbers are defined in the usual way as

$$Re = \frac{\rho V D}{\mu}, \quad We = \frac{\rho V^2 D}{\sigma}, \quad Pe = \frac{VD}{\alpha}. \tag{33}$$

Additionally, the aspect ratio $\mathcal{A} = H/D$ is a relevant nondimensional parameter. The overpressure Δp is taken as the difference between the saturation pressure corresponding to the initial surface temperature and the ambient pressure p_∞.

The simulations presented below have been carried out for a tube with a diameter of 50 μm and an aspect ratio $\mathcal{A} = 20$ so that the liquid column half-length is 1 mm. In order to limit the computational effort, this value for the aspect ratio is smaller than those used in the experiments presented in [52], which were of the order of 500. Thus, we will only attempt a qualitative comparison with experiment.

Due to the small aspect ratio, the actual physical properties of water would result in fairly large *Re* and *Pe* numbers which would, in turn, require a fine discretization to resolve the associated thin thermal boundary layers. We therefore selected the liquid viscosity and thermal diffusivity so that the non-dimensional numbers are roughly the same as those in the experiments. The properties for the liquid were chosen as $\rho = 10^3$ kg/m^3, $\mu = 1.4 \times 10^{-3}$ kg/m s, $\sigma = 0.073$ N/m, $\alpha = 8.5 \times 10^{-7}$ m^2/s, $L = 2257$ kJ/kg and $Pr = \mu/\rho\alpha = 1.64$. The reference pressure at the tube end is $p_\infty = 101$ kPa and the reference temperature at the top boundary of the energy domain is $T_\infty = 25$ °C.

The bubble nucleation process depends on non-deterministic thermodynamic fluctuations and cannot be included in the numerical simulation. The computations are started from a spherical bubble with a diameter $2R_0$ equal to 20 μm, namely

40% of the tube diameter, centered on the cylinder axis at the mid-point of the column. For the same reason described earlier, an initial liquid temperature distribution is assumed given by the Gaussian function

$$T(r,z,0) = T_\infty + \Delta T \exp\left[-\left(\frac{\sqrt{r^2+z^2}-R_0}{\delta}\right)^2\right], \tag{34}$$

where ΔT is the difference between the initial vapor temperature and T_∞ and δ is the thermal boundary layer thickness. The effects of different choices for ΔT and δ are studied in [24]. Here, for purposes of illustration, we only consider one case with $\delta/R_0 = 0.75$; the momentum grid spacing is $\Delta r/D = \Delta z/D = 0.0156$. For the initial superheat, as suggested by experiment [52], we take $\Delta T = 145$ °C with a corresponding vapor pressure $p_v(0) = 7.97 \times 10^5$ Pa. The velocity scale is $V = 5.9$ m/s and the time scale $t_s = 8.48$ μs. The resulting non-dimensional numbers are $Re = 212$, $We = 24.2$ and $Pe = 349.7$.

5.2. Thermal grid refinement

Fig. 13 shows the results of the simulation for the bubble length, interface velocity, vapor temperature and pressure as functions of time. The bubble length is defined as the distance from the center of the initial bubble to the intersection of the bubble surface with the tube axis of symmetry and the interface velocity as the velocity of this point. The lines in the figure correspond to four different thermal grid spacings, $\Delta r_{therm}/\Delta r = 1/2$ (dash-and-dots), 1/4 (dotted), 1/8 (dashed) and 1/16 (solid). It can be seen that, for these quantities, grid independence does not require a very large refinement due to the moderate Re and Pe numbers.

The effect of the thermal grid refinement is seen more clearly in the calculation of the total heat flow out of the liquid given by

$$\oint k\nabla T \cdot \mathbf{n} dS, \tag{35}$$

where S is the bubble surface. This quantity is positive when heat flows prevalently out of the liquid and negative otherwise. Fig. 14 shows the sensitivity of this heat flow to the thermal grid resolution upon the refinement of which the oscillations strongly decrease.

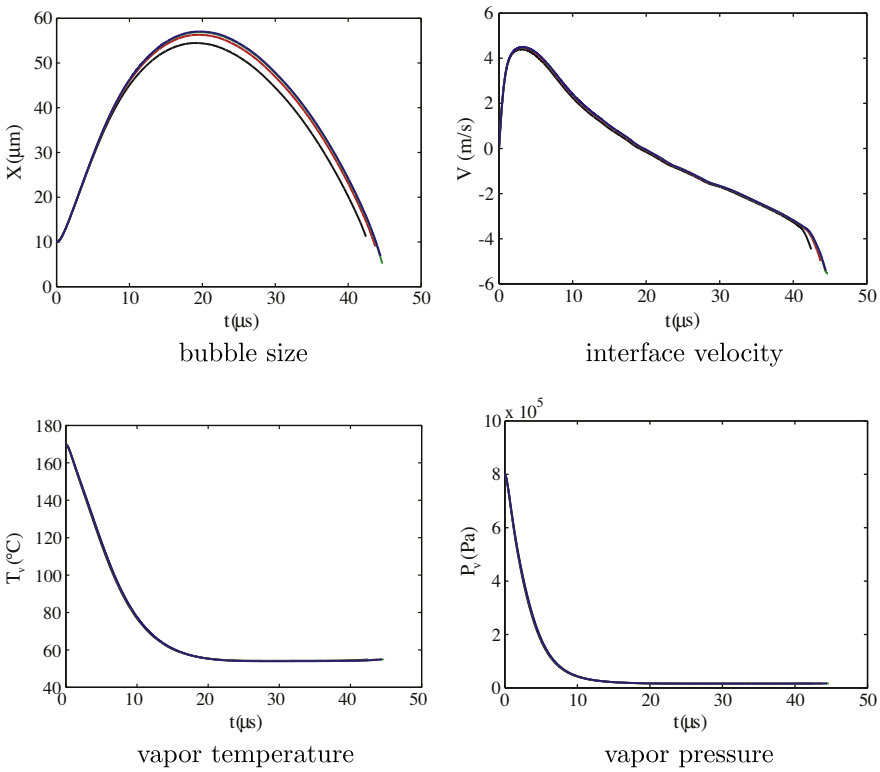

Fig. 13. Simulation results for various quantities upon refining the energy grid; dashed-dotted line, $\Delta r_{therm}/\Delta r = 1/2$; dotted line, $\Delta r_{therm}/\Delta r = 1/4$; dashed line, $\Delta r_{therm}/\Delta r = 1/8$; solid line, $\Delta r_{therm}/\Delta r = 1/16$.

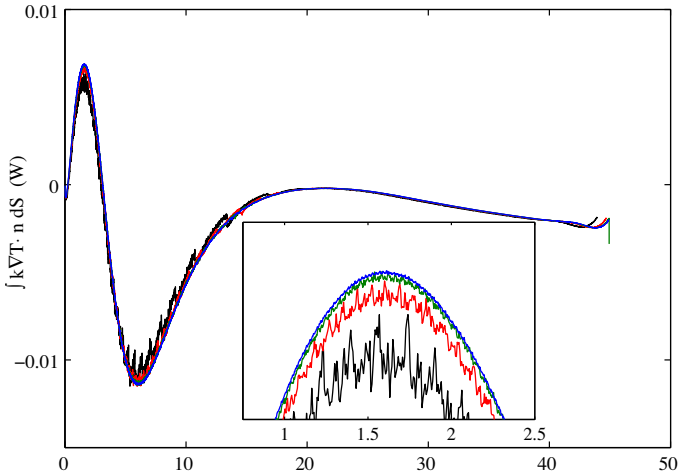

Fig. 14. Total conductive energy flux at the interface, $\oint k\nabla T \cdot \mathbf{n} dS$. This particular quantity is very sensitive to the computation of the thermal gradient at the interface. Here the value of the integral is shown as a function of time for successively larger refinements of the thermal grid. Black, $\Delta r_{therm}/\Delta r = 1/2$; red, $\Delta r_{therm}/\Delta r = 1/4$; green, $\Delta r_{therm}/\Delta r = 1/8$; blue, $\Delta r_{therm}/\Delta r = 1/16$. (For interpretation of the references to colour in this figure legend, the reader is referred to the web version of this article.)

5.3. Qualitative comparison with experimental data

For the reasons explained before, we can only carry out a qualitative comparison with experimental data from [52], which are shown in Fig. 15. Qualitatively, all aspects of the data are reproduced by the numerical simulation. The initial bubble growth proceeds violently due to the large initial vapor pressure. The duration of this fast growth is short, however, as the vapor temperature and, with it, the pressure decrease quickly due to the work of expansion and vapor condensation. After this initial phase the motion proceeds largely by inertia. The slowness of the collapse relative to the growth and the high level of the vapor temperature at the end of the collapse found in the experiments and also in the one-dimensional model of [52] are reproduced.

In [54] the bubble was approximated as a cylinder occupying the entire tube cross section. The growth of the bubble was initiated by applying a constant over-pressure Δp for a certain amount of time τ_{pulse}, after which the bubble pressure was set to the very small value corresponding to the vapor pressure at the undisturbed temperature. In [53] this model was further

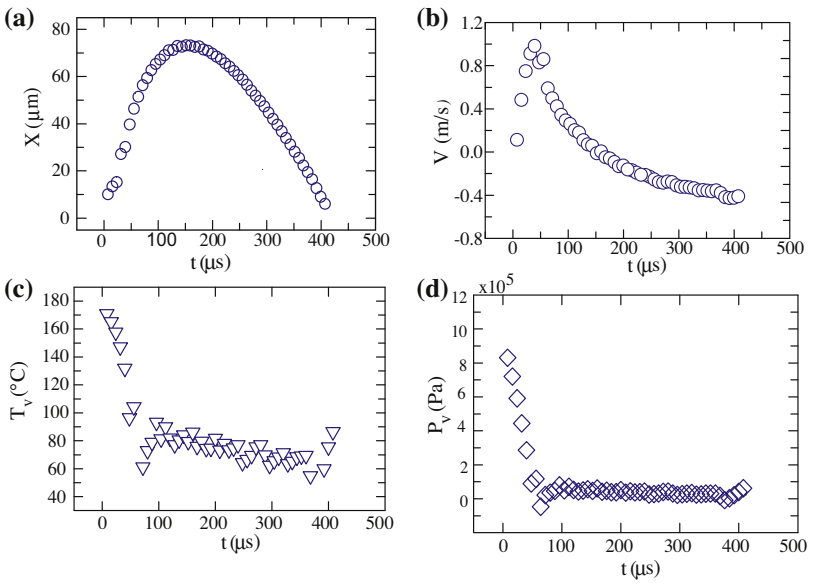

Fig. 15. Experimental results for the growth and collapse of a laser-generated vapor bubble in a microtube from [52]. Panel (a) is the bubble length, (b) the velocity of the interface point on the axis, (c) the vapor temperature and (d) the vapor pressure.

simplified by neglecting viscosity and assuming the bubble surface to remain sufficiently far from the tube ends. In this way expressions could be derived for the maximum bubble volume V_{max} and bubble lifetime:

$$\frac{V_{max}}{\frac{1}{4}\pi D^2 L} \simeq \frac{\Delta p \tau_{pulse}}{p_\infty} \frac{V}{AD}, \quad t_B \simeq \frac{2\Delta p \tau_{pulse}}{p_\infty - p_0}, \tag{36}$$

where V is the previous velocity scale. To use these relations we equate $\Delta p \tau_{pulse}$ to the time integral of $p_v - p_\infty$ up to the time of maximum bubble expansion finding, for our conditions, a normalized volume of 0.056 and a lifetime of 19 μs. Our computational results give 0.07 and 45 μs, respectively, for these quantities. The difference in lifetimes is quite significant and is due to the much slower collapse found both experimentally, in the model of [52] and in our own computations, a feature which is not present in the simplified argument leading to (36). The maximum volume, on the other hand, is closer to the simple estimate (36) as it depends on the expansion phase which is dominated by inertia and the bubble internal pressure, with viscosity playing a relatively minor role.

5.4. Bubble shape and temperature field

Figs. 16 and 17 show the bubble shape, temperature field and velocity vectors at several instants during the growth and collapse, respectively. The velocity vectors are plotted for every other grid cell. The initial configuration is shown in Fig. 16(a). At $t = 0.7t_s = 5.9$ μs (panel (b)) the bubble has grown to a size comparable to the tube diameter and it starts to acquire a cylindrical shape with a rounded cap. As shown by the different temperature color bars, already at this early stage the vapor temperature has dropped by approximately 60 °C due to the work necessary to push the liquid and the fast vapor condensation. The vapor pressure has dropped to almost atmospheric and the maximum velocity has already been reached. The rest of the motion is governed by inertia. The flow field is primarily directed in the axial direction and, apart from the thin viscous boundary layer at the tube wall, it is nearly uniform over the tube cross-section. In the early growth stages the thermal boundary layer is squeezed toward the wall and compressed.

Panel (c) shows the bubble at its maximum size at $t = 2.4t_s = 20.2$ μs. The surface of the bubble adjacent to the tube wall is not completely flat, but slightly convex toward the axis of symmetry. This feature was also found in the isothermal calculations of [53,55] and is due to a small pressure gradient along the wall. Due to the boundary layer nature of the wall region, the velocity near the wall has already reversed while the liquid near the axis is still moving outward. A small mass of liquid near the bubble cap hotter than the bubble by about 8 °C can also be noted in this figure. This is in part a residue of the thermal energy associated with the initial Gaussian temperature distribution and in part due to the heat released by the early

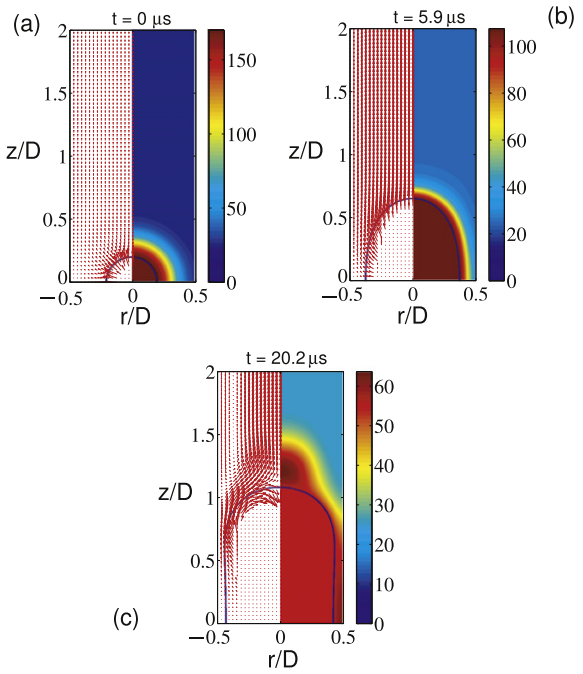

Fig. 16. Snapshots of the simulation of a laser-generated vapor bubble growing in a microtube. (a) Initial configuration; at $t = 5.9$ μs (b) the bubble has grown to a size comparable to the tube diameter, the vapor pressure has dropped to almost atmospheric and the liquid temperature has decreased significantly. The rest of the motion proceeds essentially by inertia. At $t = 20.2$ μs (c) the bubble has reached its maximum size and the fluid flow is starting to reverse.

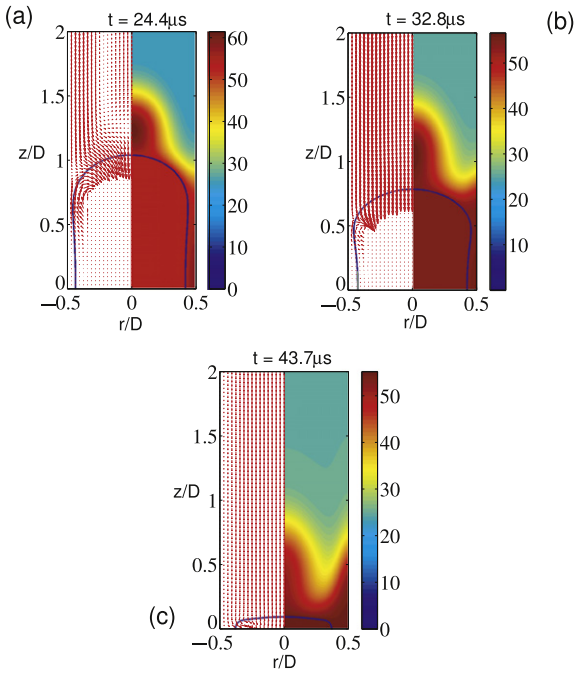

Fig. 17. Snapshots of the simulation of the collapse of the laser-generated vapor bubble of the previous figure. At $t = 24.4$ μs (a) the velocity field is almost completely reversed. At $t = 32.8$ μs (b) a tongue of cold liquid starts to separate from the hotter fluid above the bubble and the tube wall. At $t = 43.7$ μs (c) the cold liquid has nearly reached the plane of symmetry.

vapor condensation. At the time of this image, the vapor temperature has already decreased substantially and, therefore, the bubble is colder than this liquid spot. It may also be noted that, due to the cylindrical geometry, the amount of liquid constituting this hot spot is actually smaller than it appears in the image.

The collapse of the bubble is shown in Fig. 17 at times $t = 2.9t_s = 24.4$ μs, $t = 3.9t_s = 32.8$ μs and $t = 5.3t_s = 43.7$ μs. The bubble shape remains similar until the very late stages. The slight convexity toward the axis near the tube wall persists for most of the collapse. As shown in panel (c) of Fig. 13, the vapor temperature and pressure are close to their final values throughout the collapse. In panel (b) one notes the beginning of a tongue of relatively cold liquid, which is more evident in panel (c), that separates the warmer liquid near the axis noted before from the liquid near the wall in which the latent heat deposited has been trapped by the adiabatic wall condition.

6. Conclusions

We have described a computational method suitable for the simulation of vapor–liquid (or gas–liquid) flows in which the dynamical effects of the vapor can be approximated by imposing a time-dependent, spatially uniform pressure on the interface. The simplification rendered possible by this approximation enables us to develop a very accurate numerical procedure while maintaining the numerical method reasonably simple. We have also shown how the use of a finer grid for the energy equation limits the computational effort needed for an accurate computation of momentum effects while, at the same time, permitting a precise estimate of the crucial interfacial evaporation and condensation mass fluxes which drive the flow. Verification and grid refinement tests show that our method is first-order accurate in time and second-order accurate in space, as intended.

As an illustration of the capabilities of the computational procedure we have simulated the growth and subsequent collapse of the vapor bubble generated by a laser pulse focused on the mid-point of a liquid-filled microtube. The results provide an illuminating insight into the time evolution of the liquid temperature and of the bubble shape. Further results on this problem will be found in [24].

Acknowledgments

This work is part of the research program of the Technology Foundation STW, which is financially supported by the 'Nederlandse Organisatie voor Wetenschappelijk Onderzoek (NWO)'. The same organization also supported the dissertation work of the first author reported in [24].

Appendix A. Bubble internal pressure

Conservation of energy at the liquid–vapor interface can be expressed as

$$(\mathbf{q}-\mathbf{q}_v)\cdot\mathbf{n} = L\rho_v(\mathbf{u}_v-\mathbf{v})\cdot\mathbf{n} \equiv L\dot{m}, \tag{A.1}$$

where $\mathbf{u}_v$ is the vapor velocity at the interface, $\mathbf{v}$ the interface velocity, $\dot{m}$ the local mass flux due to phase change and $\mathbf{q} = -k\mathbf{n}\cdot\nabla T$ is the heat flux with k the thermal conductivity. We assume that the vapor volume V is a closed and finite region in space. Integration over the surface S of this volume gives

$$L\oint \dot{m}dS = L\frac{d}{dt}(\rho_v V) = \oint(\mathbf{q}-\mathbf{q}_v)\cdot\mathbf{n}dS, \tag{A.2}$$

where, in the first step, we have assumed the vapor density to be spatially uniform. Using the estimate of the heat flux on the vapor side derived in [51] this equation can be written as

$$L\frac{d}{dt}(\rho_v V) + \rho_v V c_s\frac{dT_s}{dt} = \oint k(\nabla T\cdot\mathbf{n})dS, \tag{A.3}$$

where $c_s = c_{pv} - L/T_s$ is the vapor specific heat along the saturation line. The vapor specific heat at constant pressure, c_{pv}, is treated as a constant as are the other thermal properties. The first term in the left hand side of (A.3) represents the latent heat associated with phase change, the second term represents the change of the vapor enthalpy along the saturation line and the right hand side represents the heat flux on the liquid side.

Conservation of mass at the interface is expressed by

$$\dot{m} = \rho_v(\mathbf{u}_v-\mathbf{v})\cdot\mathbf{n} = \rho(\mathbf{u}-\mathbf{v})\cdot\mathbf{n} \tag{A.4}$$

from which

$$\mathbf{u}\cdot\mathbf{n} = \mathbf{v}\cdot\mathbf{n} + \frac{\rho_v}{\rho}(\mathbf{u}_v-\mathbf{v})\cdot\mathbf{n} \simeq \mathbf{v}\cdot\mathbf{n}, \tag{A.5}$$

in view of the smallness of ρ_v/ρ. Upon using this approximation, the equation of state for the vapor and the Clausius–Clapeyron relation, (A.3) can be written as (8) in the text.

References

[1] S. Welch, J. Wilson, A volume of fluid based method for fluid flows with phase change, J. Comput. Phys. 160 (2000) 662–682.
[2] G. Tomar, G. Biswas, A. Sharma, A. Agrawal, Numerical simulation of bubble growth in film boiling using a coupled level-set and volume-of-fluid method, Phys. FLuids 17 (2005) 112103.
[3] S.O. Unverdi, G. Tryggvason, A front-tracking method for viscous, incompressible, multi-fluid flows, J. Comput. Phys. 100 (1992) 25–37.
[4] R.P. Fedkiw, T. Aslam, B. Merriman, S. Osher, A non-oscillatory Eulerian approach to interfaces in multimaterial flows (the Ghost Fluid Method), J. Comput. Phys. 152 (1999) 457–492.
[5] F. Gibou, L. Chen, D. Nguyen, S. Banerjee, A level set based sharp interface method for the multiphase incompressible Navier–Stokes equations with phase change, J. Comput. Phys. 222 (2007) 536–555.
[6] R. Scardovelli, S. Zaleski, Direct numerical simulation of free-surface interfacial flow, Ann. Rev. Fluid. Mech. 31 (1999) 567–603.
[7] G. Son, A level set method for incompressible two-fluid flows with immersed solid boundaries, Numer. Heat Transf. B47 (2005) 473–489.
[8] M.M. Francois, S.J. Cummins, E.D. Dendya, D.B. Kothe, J.M. Sicilian, M.W. Williams, A balanced-force algorithm for continuous and sharp interfacial surface tension models within a volume tracking framework, J. Comput. Phys. 213 (2006) 141–173.
[9] S. Popinet, S. Zaleski, A front-tracking algorithm for accurate representation of surface tension, Int. J. Numer. Methods Fluids 30 (1999) 775–793.
[10] G. Son, V.K. Dhir, A level set method for analysis of film boiling on an immersed liquid surface, Numer. Heat Transf. B52 (2007) 153–177.
[11] G. Son, V.K. Dhir, Numerical simulation of nucleate boiling on a horizontal surface at high heat fluxes, Int. J. Heat Mass Transf. 51 (2008) 2566–2582.
[12] J.F. Wu, V.K. Dhir, Numerical simulations of the dynamics and heat transfer associated with a single bubble in subcooled pool boiling, J. Heat Transf. 132 (2010) 111501.
[13] A. Asai, T. Hara, I. Endo, One-dimensional model of bubble growth and liquid flow in bubble jet printers, Japan. J. Appl. Phys. 26 (1987) 1794–1801.
[14] A. Asai, Application of the nucleation theory to the design of bubble jet printers, Japan. J. Appl. Phys. 28 (1989) 909–915.
[15] R.R. Allen, J.D. Meyer, W.R. Knight, Thermodynamics and hydrodynamics of thermal ink jets, Hewlett-Packard J. 36 (1985) 21–27.
[16] A. Asai, Bubble dynamics in boiling under high heat flux pulse heating, J. Heat Transf. 113 (1991) 973–979.
[17] L. Lin, A.P. Pisano, A.P. Lee, Microbubble powered actuator, in: Proceedings of the International Conference on Solid-State Sensors and Actuators, 1991, pp. 1041–1044.
[18] D.M. van den Broek, M. Elwenspoek, Explosive micro-bubble actuator, Proc. Transducers 2 (2007) 2441.
[19] J. Tsai, L. Lin, A thermal-bubble-actuated micronozzle-diffuser pump, J. Microelectromech. Syst. 11 (2002) 665–671.
[20] Z. Yin, A. Prosperetti, J. Kim, Bubble growth on an impulsively powered microheater, Int. J. Heat Mass Transf. 47 (2004) 1053–1067.
[21] C.D. Ohl, M. Arora, R. Dijkink, V. Janve, D. Lohse, Surface cleaning from laser-induced cavitation bubbles, Appl. Phys. Lett. 89 (2006) 074102.
[22] S. Popinet, S. Zaleski, Bubble collapse near a solid boundary: a numerical study of the influence of viscosity, J. Fluid Mech. 464 (2002) 137–163.
[23] M. Sussman, A second order coupled level set and volume-of-fluid method for computing growth and collapse of vapor bubbles, J. Comput. Phys. 187 (2003) 110–136.
[24] E. Can, Vapor bubbles in confined geometries: a numerical study, Ph.D. thesis, Department of Applied Physics, Physics of Fluids Chair, University of Twente, The Netherlands.
[25] J.A. Sethian, P. Smereka, Level set methods for fluid interfaces, Ann. Rev. Fluid Mech. 35 (2003) 341–372.
[26] S. Osher, R. Fedkiw, Level Set Methods and Dynamic Implicit Surfaces, Springer-Verlag, New York, 2003.
[27] A. Harten, B. Engquist, S. Osher, S. Chakravarthy, Uniformly high order accurate essentially non-oscillatory schemes III, J. Comput. Phys. 71 (1987) 231–303.
[28] S. Osher, J. Sethian, Fronts propagating with curvature dependent speed: algorithms based on Hamilton–Jacobi formulations, J. Comput. Phys. 79 (1988) 12–49.

[29] S. Osher, C.W. Shu, High order essentially non-oscillatory schemes for Hamilton–Jacobi equations, SIAM J. Numer. Anal. 28 (1991) 902–921.
[30] C.W. Shu, S. Osher, Efficient implementation of essentially non oscillatory shock capturing schemes, J. Comput. Phys. 77 (1988) 439–471.
[31] C.W. Shu, S. Osher, Efficient implementation of essentially non oscillatory shock capturing schemes II, J. Comput. Phys. 83 (1989) 32–78.
[32] G.S. Jiang, D. Peng, Weighted ENO schemes for Hamilton Jacobi equations, SIAM J. Sci. Comput. 21 (2000) 2126–2143.
[33] G.S. Jiang, C.W. Shu, Efficient implementation of weighted ENO schemes II, J. Comput. Phys. 126 (1996) 202–228.
[34] M. Sussman, P. Smereka, S. Osher, A level set approach for computing solutions to incompressible two-phase flow, J. Comput. Phys. 114 (1994) 146–159.
[35] M. Sussman, E. Fatemi, An efficient, interface-preserving level set redistancing algorithm and its applications to interfacial incompressible fluid flow, SIAM J. Sci. Comput. 20 (1999) 1165–1191.
[36] G. Russo, P. Smereka, A remark on computing distance functions, J. Comput. Phys. 163 (2000) 51–67.
[37] D. Enright, R. Fedkiw, J. Ferziger, I. Mitchell, A hybrid particle level set method for improved interface capturing, J. Comput. Phys. 183 (2002) 83–116.
[38] A. du Chene, C. Min, F. Gibou, Second order accurate computation of curvatures in a level set framework using novel high order reinitialization schemes, SIAM J. Sci. Comput. 35 (2007) 114–131.
[39] R. Verzicco, P. Orlandi, A finite-difference scheme for three-dimensional incompressible flows in cylindrical coordinates, J. Comput. Phys. 123 (1995) 402–414.
[40] A.J. Chorin, Numerical solution of the Navier–Stokes equations, Math. Comput. 22 (1968) 745.
[41] J.H. Ferziger, M. Perić, Computational Methods for Fluid Dynamics, third ed., Springer, 2002.
[42] P. Wesseling, Principles of Computational Fluid Dynamics, Springer, 2001.
[43] F. Gibou, R.P. Fedkiw, L. Cheng, M. Kang, A second order accurate symmetric discretization of the Poisson equation on irregular domains, J. Comput. Phys. 176 (2002) 205–227.
[44] S. Tanguy, T. Ménard, A. Berlemont, A level set method for vaporizing two-phase flows, J. Comput. Phys. 221 (2007) 837–853.
[45] T. Aslam, A partial differential equation approach to multidimensional extrapolation, J. Comput. Phys. 193 (2004) 349–355.
[46] M.S. Plesset, A. Prosperetti, Bubble dynamics and cavitation, Ann. Rev. Fluid. Mech 9 (1977) 145–185.
[47] A. Prosperetti, Bubbles, Phys. Fluids 16 (2004) 1852–1865.
[48] B. Yang, A. Prosperetti, A second-order boundary-fitted projection method for free-surface flow computations, J. Comput. Phys. 213 (2006) 574–590.
[49] L. Florschuetz, B. Chao, On the mechanics of vapour bubble collapse, J. Heat. Transf. 87 (1965) 209–220.
[50] Y. Hao, A. Prosperetti, The collapse of vapor bubbles in a spatially non-uniform flow, Int. J. Heat Mass Transf. 43 (2000) 3539–3550.
[51] B. Yang, A. Prosperetti, Vapour bubble collapse in isothermal and non-isothermal liquids, J. Fluid Mech. 601 (2008) 253–279.
[52] C. Sun, E. Can, R. Dijkink, D. Lohse, A. Prosperetti, Growth and collapse of a vapor bubble in a microtube: the role of thermal effects, Phys. Rev. Lett. 632 (2007) 5–16.
[53] E. Ory, H. Yuan, A. Prosperetti, S. Popinet, S. Zaleski, Growth and collapse of a vapor bubble in a narrow tube, Phys. Fluids 12 (2000) 1268–1277.
[54] H. Yuan, A. Prosperetti, The pumping effect of growing and collapsing bubbles in a tube, J. Micromech. Microeng. 9 (1999) 402–413.
[55] T. Ye, J.L. Bull, Direct numerical simulations of micro-bubble expansion in gas embolotherapy, ASME J. Biomech. Eng. 126 (2004) 745–759.